https://doi.org/10.5194/acp-2022-786
Preprint. Discussion started: 16 December 2022

Atmospheric Chemistry and Physics Discussions
Open Access
EGU

In-depth study of the formation processes of single atmospheric particles in the southeastern margin of Tibetan Plateau

Li Li[1,3], Qiyuan Wang[1,2], Jie Tian[1], Huikun Liu[1], Yong Zhang[1], Steven Sai Hang Ho[4], Weikang Ran[1], Junji Cao[5]

[1] Key Laboratory of Aerosol Chemistry and Physics, State Key Laboratory of Loess and Quaternary Geology, Institute of Earth Environment, Chinese Academy of Sciences, Xi'an 710061, China
[2] CAS Center for Excellence in Quaternary Science and Global Change, Xi'an 710061, China
[3] University of Chinese Academy of Sciences, Beijing 100049, China
[4] Division of Atmospheric Sciences, Desert Research Institute, Reno, NV 89512, United States
[5] Institute of Atmospheric Physics, Chinese Academy of Sciences, Beijing 100029, China

Correspondence to: Qiyuan Wang (wangqy@ieecas.cn) and Junji Cao (jjcao@mail.iap.ac.cn).

https://doi.org/10.5194/acp-2022-786
Preprint. Discussion started: 16 December 2022

Atmospheric Chemistry and Physics Discussions

Abstract

The unique geographical location of the Tibetan Plateau (TP) plays an important role in regulating global climate change, but the impacts of the chemical components and atmospheric processing on the size distribution and mixing state of individual particles are rarely explored in the southeastern margin of the TP, which is a transport channel for pollutants from Southeast Asia during the pre-monsoon season. Thus a single-particle aerosol mass spectrometer (SPAMS) was deployed to investigate how the local emissions of chemical composition interact with the transporting particles and assess the mixing state of different particle types and secondary formation in this study. The TP particles were classified into six main types: the rich-potassium (rich-K) type was the largest fraction of the total particles (30.9%), followed by the biomass burning (BB) type (18.7%). Most particle types were mainly transported from the surroundings and cross-border of northern Myanmar; but the air masses from northeastern India and Myanmar show a greater impact on the number fraction of BB (31.7%) and Dust (18.2%) types, respectively. Besides, the two episodes events with high particle concentrations showed that the differences in the meteorological conditions in the same air clusters could cause significant changes in chemical components, especially the Dust and EC-aged types changed by a sum of 93.6% and 72.0% respectively. Ammonium and Dust particles distribute at a relatively larger size (~ 600 nm), but the size peak of other types is present at ~ 440 nm. The easily volatilized nitrate ($^{62}NO_3^-$) during the transport process leads the more abundant sulfate ($^{97}HSO_4^-$) to mix internally with the TP particles. $C_2H_3O^+$, $HC_2O_4^-$, NH_4^+, NO_3^-, and HSO_4^-, severed as the indicators of secondary formation, are present in the atmospheric aging process of photo-oxidation and aqueous reaction by a linear correlation with O_x (O_3+NO_2) and relative humidity (RH). This study provides insights that can improve the knowledge of particle composition and size, mixing state, and aging mechanism at high time resolution over the TP region.

Keywords

Southeastern Tibetan Plateau, Pre-monsoon, Individual particles, Chemical characteristics, Atmospheric aging,

https://doi.org/10.5194/acp-2022-786
Preprint. Discussion started: 16 December 2022

1 Introduction

Atmospheric aerosols have complex components and sources and can be coated with inorganic or organic materials during transport and atmospheric processing (Crippa et al., 2013). When further coated through coagulation, condensation, and photochemical oxidation, their physical and chemical properties and optical properties will change greatly, making their impact on the air more uncertain (Jacobson, 2002; Zaveri et al., 2010; Matsui, 2016; Budisulistiorini et al., 2017). The ability of aerosol particles to affect atmospheric conditions is dependent on their sizes, chemical compositions, and mixing states (Mc Figgans et al., 2006; Dusek et al., 2006; Ma et al., 2012). For example, dust aerosol is an important factor affecting climate change through the interactions of various physical processes such as the direct radiative effect (Mahowald et al., 2014; Shao et al., 2011; Wang et al., 2022); the formation of secondary chemical components often aggravates regional pollution. However, the ability of secondary formation has regional differences due to the variations in precursors, source strengths, and meteorological conditions (Pratt et al., 2011; Volkamer et al., 2006). The influence of these complex chemical components on aerosol size and mixing state varies with the pollution sources and/or atmospheric formation mechanism, which have been widely studied in urban of low altitude (Pratt et al., 2011; Liu et al., 2020a; Xu et al., 2017). Furthermore, a previous study found that the migration or formation of low-volatile component (such as nitrate and organic matter) could effectively be reduced due to evaporation during the upward transportation process (Liu et al., 2020b), which further alter the chemical compositions and the particle sizes. In addition, the transportation of the aerosols to a relatively cleaner environment prevails the formation of secondary chemicals at a high altitude (Liu et al., 2020b). Therefore, a comprehensive investigation of the detailed characteristic of aerosol formation and mixing states is required to understand their environmental effects in low-, and high-altitude.

As a typical high-altitude region, the Tibetan Plateau (TP) has the highest and largest mountain area in the world, which is the most sensitive and obvious indicator of climate change in the entire Asian continent (Yao, et al., 2012; Chen and Bordoni, 2014; Immerzeel et al., 2010). In recent decades, many studies have shown that the melting and retreat of glaciers

https://doi.org/10.5194/acp-2022-786
Preprint. Discussion started: 16 December 2022

in the TP regions is accelerating, and the main reason is attributable to anthropogenic emissions, such as greenhouse gases and aerosols (William et al., 2010; Luo et al., 2020; Hua et al., 2019). Atmospheric aerosols also can influence the properties and life span of clouds as cloud condensation nuclei, and affect local hydrological cycles and monsoon patterns by changing the microphysical properties of clouds (Qian et al., 2011; Seinfeld and Pandis, 2012, Xia et al., 2007; Gettelman et al., 2013; Kumar et al., 2017). The southern part of the TP is always affected by the transport of more polluted air from South Asia along the mountain valleys, especially during the pre-monsoon (i.e., March-May) with the southwest prevailing wind (Cao et al., 2010; Chan et al., 2017; Zhu et al., 2017; Zhao et al., 2017; Han et al., 2020). Most studies have focused on the influence of optical properties; however, a few studies have been conducted on aerosol components within the plateau.

Present aerosol components studies conducted in TP mostly focus on exploring the influence of light-absorbing carbon aerosols and dust particles on climate change by optical or offline sampling methods (e.g., Wang et al., 2019a; Liu et al., 2021). There is a lack of studies on the full composition, mixing states, and formation mechanism of aerosols in the southeast margin and even the entire TP, especially using high-time resolved measurements. Although time-integrated sampling with filter collection followed by laboratory analyses has been widely adopted for the chemical characterization of aerosols (Chen et al., 2015; Li et al., 2022a; Shen et al., 2015; Zhang et al., 2013). Drawbacks of the traditional approach include low time resolution, high detection limit, and time- and labor-intensive procedures. More advanced aerosol online measurement devices with a high temporal resolution, such as the aerosol chemical speciation monitor (ACSM) and aerosol mass spectrometer (AMS) (Ng et al., 2011; Canagaratna et al., 2007) show the inability to measure the mixing state of particles and limit to obtain the information of non-refractory submicron aerosol. AMS/ACSM mainly used to provide online observation datasets with high temporal resolution (including the mass concentration of sulfate, nitrate, ammonium, chloride, and organic; and corresponding mass spectral), which is beneficial to obtain the dynamic processes of source emission in the atmosphere (Du et al., 2015; Zhang et al., 2019a). At the same time, aerosol time-of-flight mass spectrometry (ATOFMS) (Prather et al., 1994), and single particle aerosol mass spectrometer (SPAMS) (Li et al., 2011), are popular for characterizing atmospheric individual

https://doi.org/10.5194/acp-2022-786
Preprint. Discussion started: 16 December 2022

particles. These devices could determine the full chemical composition and their size distribution, to achieve more detailed information, such as the dynamic processes of chemical aging, mixing state, and transport of the aerosols (Wang et al., 2016; Zhang et al., 2015, 2016). To the best knowledge, the advanced measurement device has not yet been applied for the studies conducted in TP, leading to a lack of in-depth research on the $PM_{2.5}$ pollution in TP, especially in the southeastern margin. The shortage of information hinders our understanding of the distribution characteristics and formation mechanism of full aerosol components in high-altitude regions.

The southeastern margin of the TP is an important transitional zone between the high-altitude TP and the low-altitude Yungui Plateau (Wang et al., 2019a; Zhao et al., 2017), an ideal place for investigating the impacts of pollutants transport and formation in the high-altitude zone. In this study, a high-time resolution field observation of individual particles (SPAMS) was deployed on the southeastern margin of the TP during the pre-monsoon, to continuously (i) investigate the changes of chemical characteristics between transport and local fine particles during pre-monsoon, (ii) determine the particle size distributions, and the mixing states of different particle types, and (iii) assess the contributions of photooxidation and aqueous reaction to the formation of the secondary species. These results would expand our understanding of the chemical components, size distribution, mixing state, and aging pathways of aerosols in the high-altitude areas in the TP and surrounding areas.

2 Methodology

2.1 Observation site

Intensive 1-month field observation was deployed at the rooftop (~ 10 m above the ground) of the Lijiang Astronomical Station, Chinese Academy of Sciences (3260 m above sea level; 26°41′24″N, 100°10′48″E), Gaomeigu County, Yunnan Province, China, during the pre-monsoon period (from April 14th to May 13th, 2018). The nearest residential area is the Gaomeigu village (3–5 km away) with a small population size of 113 residents in 27 households. The villagers make a living by farming (e.g., potato and autumn rape), and biomass is the main residential fuel (Li et al., 2016). The site is surrounded by rural and

https://doi.org/10.5194/acp-2022-786
Preprint. Discussion started: 16 December 2022

mountainous areas and has no obvious industry or traffic emissions. During the observation period, the average temperature (T) and relative humidity (RH) are 8.4 ± 3.1℃ and 69% ± 21%, respectively. The wind speed (WS) is 2.2 ± 1.2 $m \cdot s^{-1}$ with the prevailing wind in the north and northeastern (Fig. S1).

2.2 On-line instrument

A detailed operational principle and the calibrations of the single-particle aerosol mass spectrometer (SPAMS, Hexin Analytical Instrument Co., Ltd., Guangzhou, China) has been described elsewhere (Li et al., 2011). Briefly, individual particles are drawn into SPAMS through a critical orifice. The particles are focused and accelerated, then aerodynamically sized by two continuous diode Nd: YAG laser beams (532 nm), subsequently desorbed and ionized by a pulsed laser (266 nm) triggered exactly based on the velocity of the specific particle. The generated of positive and negative molecular fragments are recorded with the corresponding size of individual particles. In summary, a velocity, a detection moment, and an ion mass spectrum are recorded for each ionized particle, while there is no mass spectrum for not ionized particles. The velocity could be converted to d_{va} based on a calibration using polystyrene latex spheres (PSL, Thermo Scientific Corp., Palo Alto, USA) with predefined sizes. The average ambient pressure is 690 hPa (in a range of 685–694 hPa) during the measurements and calibration. Particles measured by SPAMS mostly are within the size range of vacuum aerodynamic diameter (d_{va}) 0.2–2.0 μm.

Meteorological parameters, including the planetary boundary layer (PBL), temperature (℃), RH (%), WS ($m \cdot s^{-1}$), and wind direction (WD) were continuously achieved using an automatic weather station (Model MAWS201, Vaisala HydroMet, Helsinki, Finland) at a time resolution of 5 min. Gaseous concentrations (ppbv) were obtained using a multiple gas analyzer (Thermo Scientific Corp.), including ozone (O_3, model 49i) and nitrogen oxides (NO_x, model 42i) in a 5-min resolution. The SPAMS and gas analyzers are co-located in the same position, while the weather station was uncovered outside ~5 m from the sampling house. Time series of SPAMS particles, gaseous concentrations (NO, NO_x, O_3, and CO) and meteorological parameters (PBL, temperature, RH, WD, and WS) were shown in Fig. S2.

2.3 Individual particle classification

https://doi.org/10.5194/acp-2022-786
Preprint. Discussion started: 16 December 2022

During the observation period, a total of 461,876 ambient particles with the size (d_{va}) of 0.2–2.0 μm were collected, including 55,583 in Episode I (E1; from April 18th 08:00 to April 19th 08:00) and 62,110 in Episode II (E2; from April 26th 17:00 to April 28th 02:00). The analyzed particles are classified into 1,557 clusters using an adaptive resonance theory neural network (ART-2a) with a vigilance factor of 0.8, a learning rate of 0.05, and 20 iterations (Song et al., 1999). Finally, eight major particle clusters [i.e., Potassium-rich (rich-K), Biomass Burning (BB), Organic Carbon (OC), Ammonium, Aging Element Carbon (EC-aged), Dust, Sodium, Potassium-containing (NaK-SN), and Iron (Fe)-Lead (Pb)-containing (Metal)] with distinct chemical patterns were manually combined, which represent ~99.7 % of the population of the detected particles. The remaining particles are grouped as "Other". The characteristics of the positive and negative mass spectra (MS) of each particle type are shown in Fig. S3. A detailed description of classification criteria for individual particles and the characteristic ion fragments for each particle type can be found in Text S1.

2.4 Trajectory-related analysis

To determine the influence of regional transport on different particles at Gaomeigu, the trajectory clusters analysis was carried out using the 72-h backward air mass trajectories at 500 m above the ground level. The trajectories were calculated with the Hybrid Single-Particle Lagrangian Integrated Trajectory model (Draxler and Hess, 1998), and the meteorological data were obtained from the Global Data Assimilation System (GDAS; ftp://arlftp.arlhq.noaa.gov/pub/archives/gdas1, last access: 6 April, 2022). The cluster analysis employs a Euclidean-oriented distance definition to differentiate and cluster the major spatial features of the inputting trajectories. Details of the trajectory clustering method can be found in Sirois and Bottenheim (1995). To investigate the effects of transport on the chemical characteristic of the individual particles, trajectories with particle number concentrations high than the 75th percentile are considered as pollution (Liu et al., 2021).

3 Results and Discussion

3.1 Characteristics of particle composition

https://doi.org/10.5194/acp-2022-786
Preprint. Discussion started: 16 December 2022

Table 1 summarizes the numbers of concentrations, relative percentages, and characteristic ions of each particle type. The most dominant particle type in Gaomeigu during pre-monsoon is rich-K, accounting for an average of 30.9% of the total resolved particles, followed by BB (18.7%), OC (12.8%), Ammonium (11.9%), EC-aged (10.9%), and Dust (10.7%). Similar to the results of some studies in urban areas, rich-K or carbonaceous-containing type is the dominant particle type (15-50%) (Li et al., 2014; Zhang et al., 2015; Shen et al., 2017; Zhang et al., 2017; Xu et al., 2018). Differently, few researchers can capture the high proportion of Ammonium particles as shown in this study (Shen et al., 2017; Xu et al., 2018), which is ascribed to the conversion of ammonia (NH_3) precursor emitted from large-scale agricultural activities and mountain forest (Engling et al., 2011; Li et al., 2013). It is necessary to point out that 60% of Ammonium particles contain signals of diethylamine (DEA, $^{58}C_2H_5NHCH_2^+$), implying their similar formation pathway (Zhang et al., 2012). Moreover, the DEA-containing particle represented 12.5% of the total ambient particles, which is significantly higher than that in some urban areas at low altitudes (around 2%) (Cahi et al., 2012; Pratt and Prather, 2010; Zhang et al., 2015; Li et al., 2017) but is comparable to the observed in processing of high RH, fog and cloud events at a high altitude (> 9%) (Roth et al., 2016; Lin et al., 2019). This suggests that the formation of amines under high RH and fog condition might exist in the Gaomeigu area (with an altitude of 3260 m), for example the high relative fraction of DEA-containing particle corresponds to a high RH (Fig. S4), and the existence of amine sources govern the ammonium formations (Bi et al., 2016; Rehbein et al., 2011; Zhang et al., 2012). The relatively larger fraction of Dust particles is related to the short-time occurrences of dust events in spring (Fig. S5), leading to a wide contribution ranging between 10% and 70% in the period of 19:00 on April 16th to 10:00 on April 17th.

Fig. 1 shows the diurnal variations of each particle type. The rich-K, BB, and OC particles decrease after midnight until 06:00, possibly explained by the curtailment of local traffic and biomass-burning activities even though both the planetary boundary layer (PBL) height and WS decrease (Fig. S6). Then, they rapidly increase around 07:00 when the pollutants from biomass burning are transported from the upwind region as the PBL rises (Liu et al., 2021). At 11:00, the particle counts sharply decrease till 16:00–17:00, caused by

https://doi.org/10.5194/acp-2022-786
Preprint. Discussion started: 16 December 2022

the pollutant dispersion with the increases of the PBL height and WS. Increasing trends are observed after 17:00 due to the reduction of PBL height and WS. In contrast, the Ammonium, EC-aged, and Dust particles show a unimodal pattern of the daily diurnal variation (Fig. 1d–f). From 00:00 to 06:00, minor fluctuation of particle concentrations of Ammonium, EC-aged, and Dust is observed for these particle types. After that, they continuously elevate until 12:00 due to the regional transport, traffic emission, and road dust from upwind areas (Text S2). While the PBL height and WS increase continuously, the Ammonium, EC-aged, and Dust particles begin to decline from 12:00 to 17:00. The subsequent increases of these three particles after 17:00 are attributed to the reduction of PBL height, as a result of the accumulation of pollutants in the near-surface atmosphere.

Based on the transport pathways, four air masses clusters are identified to investigate the effect of regional transport on the major particle types (i.e., rich-K, BB, OC, Ammonium, EC-aged, and Dust) (Fig. 2). The most dominant air masses are Cluster 1, 3 and 4 from northeastern Myanmar, accounting for 59.8%, 33.2% and 4.6% of the total trajectories, respectively. Cluster 1 had an average percentage of 31.2%, 20.2%, 13.7%, 11.8%, 10.9%, and 6.5%, respectively, on the rich-K, BB, OC, Ammonium, EC-aged, and Dust particles. Clusters 3 and 4 had comparable contributions of BB, OC, Ammonium, and EC-aged to those of Cluster 1, but with a high contribution of Dust, which approximately 12.2% and 18.2% of Clusters 3 and 4 are referred to as dust pollution. The diurnal variations of the BB and OC fractions are similar which rapidly elevate at 07:00 (Fig. S7) due to the increased contribution of biomass burning and vehicle emissions from Cluster 1, Ammonium and EC-aged particles (peak at 07:00) caused by the effect of Cluster 1 and 3 together. The similar diurnal trend of Clusters 3 and 4 are both associated with dust contributions, which decrease at 04:00 and increase at noon. The increased nighttime particles could be attributed to the pollutant accumulation with the decreased PBL height. Cluster 2 originated from northeastern India and passes over Bangladesh. This cluster accounts for only 2.4 % of the total trajectories, in which ~30.1% and ~31.7% are mainly associated with the rich-K and BB particles, respectively. Even though Clusters 2 and 4 are composed of a small fraction of total trajectories (2.4% and 4.6 %, respectively), BB and dust particles are identified as the major

https://doi.org/10.5194/acp-2022-786
Preprint. Discussion started: 16 December 2022

pollutants, suggesting significant influences from India and northeastern Myanmar during the campaign.

3.2 Characteristics of size distribution and mixing state

Fig. 3 shows the size distributions of each particle type. Corresponding the average MS (Text S1 and Fig. S2), rich-K, BB, and OC, EC-aged particles have similar sources from vehicle emission or solid-fuel combustion, their size distribution presents at small-scale (~440 nm) (Fig. 3a). However, the relative proportion of each particle type is distinct under different sizes range, maybe due to the different atmospheric processing in ambient. For example, as shown in Fig. 3b, the percentage of rich-K increases from 17% to 44% along with the increase of particle size from 200 to 420 nm, and then decreases to <10% at 900 nm; a similar thing, the percentage of BB increases from 9% to 27% with the increasing sizes of 200 to 420 nm, and then decreases to <10% at 660 nm. However, the OC and EC-aged types are mainly distributed in relatively small sizes, the percentage of them gradually decreases from 31% and 36% to 9% when size range from ~200 to 500 and ~400 nm, respectively. Notably, the Ammonium and Dust are mainly distributed in large sizes of ~600 nm (Fig. 3a). The Ammonium particles gradually increase from 1.6% to 29% from 440 to 740 nm, then decline to <10% at 1.2 μm. The relatively large size distribution of the Ammonium type is ascribed to the intense atmospheric aging during regional transport (Text S1). The percentage of Dust particles gradually increases from 10% at 560 nm to 60% at 1.48 μm. This is consistent with consist to the fact that the dust is a coarse particle, generally formed at the roadside and fly ash.

To investigate the mixing state of the secondary species in the six main particle types, several number fractions of secondary markers (i.e., $^{97}HSO_4^-$, $^{195}H(HSO_4)_2^-$, $^{62}NO_3^-$, $^{18}NH_4^+$, $^{58}C_2H_5NHCH_2^+$ and $^{89}HC_2O_4^-$) are selected (Fig. 4). Amine particles are characterized by ion signals of amine at *m/z* $^{58}C_2H_5NHCH_2^+$ (diethylamine, DEA) (Angelino et al., 2001; Moffet et al., 2008) and sulfuric acid at *m/z* $^{195}H(HSO_4)_2^-$, which is indicative of acidic particles (Rehbein et al., 2011).

The most abundant number fraction of $^{97}HSO_4^-$ and $^{18}NH_4^+$ in Ammonium (99% and 94%) and EC-aged (92% and 31%) particles, but the proportion of $^{62}NO_3^-$ is lower (2% and

https://doi.org/10.5194/acp-2022-786
Preprint. Discussion started: 16 December 2022

7%), suggest that ammonium sulfate is not a predominant form instead of ammonium nitrate. Meanwhile, a high number fraction of $^{195}H(HSO_4)_2^-$ and DEA is also observed in Ammonium (63% and 60%) and EC-aged (4% and 19%) particles. These abundant mixtures may represent the high hygroscopicity of Ammonium and EC-aged particles, and their ability to neutralize the acidic particles of Ammonium particle (Sorooshian et al., 2007). Then, a moderate proportion of $^{97}HSO_4^-$ and $^{18}NH_4^+$ are seen on the rich-K (65%, 7%) and OC (56%, 4%) particles. In contrast, more $^{62}NO_3^-$ contributes to the rich-K (38%) and OC (68%) particles, mainly affected by vehicle emissions (Text S1). Followed by BB (18%) and Dust (6%) particles are found a low number fraction of $^{97}HSO_4^-$, the moderate $^{62}NO_3^-$ accounts for 45% of the BB particle and only 3% of the Dust particle, and $^{18}NH_4^+$ is minor (＜1%), which is suggested the degree of BB and Dust particles aging are low. In addition, representing the component of secondary organic formation, oxalate ($^{89}HC_2O_4^-$) is mainly mixed with BB (13%) and rich-K (12%) particles, because they have similar sources from biomass burning. A relatively low fraction (<5%) of the oxalate-containing particles in the OC, Ammonium, EC-aged, and Dust particles are a result of their source origins.

Our results are inconsistent with the observations in other field studies (Zhang et al., 2015; Dall'Osto and Harrison, 2012; Li et al., 2022b), in which the carbonaceous-containing particles are more mixed with sulfate than nitrate, additionally, the rich-K and Dust particles are inclined to mix with nitrate. The dissimilarity could be potentially ascribed to the high emission of sulfate from coal combustion, biomass burning, and vehicles to the rich-K, Ammonium, and EC-aged particles (Yang et al., 2017; Li et al., 2022b), and the higher loss of more volatile nitrate than sulfate during the airmass transportation.

3.3 Formation process of the high number concentration particle episodes

A more in-depth investigation of the characteristics of the main particle types in the southeastern Tibet Plateau was conducted during two episode periods when the number concentration of particles was high (i.e., E1: from 08:00 April 18th to 08:00 April 19th, 2018; E2: 17:00 April 26th to 02:00 April 28th, 2018). Even though the two episode events are mostly contributed by Cluster 1, the chemical components show significant differences (Table 1). During E1, the average fractions of the rich-K, BB, OC, Ammonium, EC-aged, and Dust particle are 29.0%, 11.5%, 8.1%, 17.5%, 10.0% and 20.3%, respectively, different from

https://doi.org/10.5194/acp-2022-786
Preprint. Discussion started: 16 December 2022

39.3%, 14.2%, 10.0%, 13.5%, 17.2%, and 1.3% respectively, during E2. It can be seen that the Dust particle is the major changed factor, which is 93.6% lower during E2 than E1, whereas the EC-aged particle shows a reversible of 72.0% higher during E2. The rich-K, BB, and, OC particles show 22.9%-35.5% differences between the two episode periods. For the air mass clusters (Fig. S8), E1 and E2 exhibit minor differences, mostly originating from northern Myanmar and the Sino-Burmese border, but not identical regions. The Dust particles that are much lower during E2 than E1 could be explained by higher WS (on average of 2.7 ± 1.0 m/s versus 0.4 ± 0.5 m/s) (Fig. S10) and PBL height (771 ± 717 m versus 560 ± 549 m). The Dust particles are mainly formed by re-suspension in the local areas. In addition, the quick thrown-up dust belongs to more coarse size particles, which are out of the detection range of the SPAMS. However, due to the larger dust particles deposited more easily under the low WS and the stagnant air conditions during E1, more suspended dust particles of small size fall in the detection range of SPAMS. Moreover, the increased PBL height and WS could speed up the transportation of pollutants from multiple sources (e.g., traffic and biomass burning emissions) to the observation site, leading to evaluate the EC-aged, rich-K, BB, and OC particles. The decreased Ammonium particle during E2 is potentially explained by the reductions in the secondary pollutant formation with declines of RH (from 73.9% ± 23.9% to 53.1% ± 14.9%), the oxidation capacities [O_3: from 82.3 ± 5.5 ppbv to 76.8 ± 8.4 ppbv; and NO_x: from, 3.9 ± 0.8 to 2.7 ± 0.8 ppb), in comparison to those during E1.

In terms of particle size distribution, the peak value of the rich-K, BB, and EC-aged show minor differences (< 80 nm) between two episode periods (Fig. 5a). Expressed in relative proportion (Fig. 5b), the rich-K and BB particles exhibit bimodal distributions, while a peak at < 300 nm affected by the primary emissions and > 300 nm associated with the aging process (Li et al., 2022b; Bi et al., 2011). In addition, compared with that during E1, rich-K particles distribute in a wider size range and remind in a high percentage (> 20%) at ~1 μm during E2 due to the atmospheric aging of the airmass. A similar aging process leads to the particle size growth of BB, OC, Ammonium, and EC-aged particles, as well as a wider size distribution. Due to relatively low concentration, the size distribution of Dust particles greatly fluctuates.

During E1, more than 50% of $^{97}HSO_4^-$ fractions are mixed in the rich-K (81%), OC

https://doi.org/10.5194/acp-2022-786
Preprint. Discussion started: 16 December 2022

(62%), Ammonium (100%), EC-aged (98%) particles (Fig. 6), lower than in BB (37%) and Dust (4%) particles. Dissimilar with E1, the number fraction of $^{97}HSO_4^-$ increases to 34% during E2, potentially associated with the enhancement by secondary formation. However, the mixing state of $^{195}H(HSO_4)_2^-$), $^{62}NO_3^-$, $NH_4^+$and oxalate fractions are similar between the two episodes events. The fractions of DEA are significantly higher in E2 than E1 for Ammonium (67% versus 31%) and EC-aged particles (48% versus 17%), mainly due to the high hygroscopic behavior (i.e., higher RH) (Sorooshian et al., 2007).

Photochemical oxidation and aqueous-phase reaction are the key formation pathways of secondary species (Robinson et al., 2007; Link et al., 2017; Xue et al., 2014; Jiang et al., 2019). Generally, the O_x ($O_3 + NO_2$) concentration and RH serve as indicators of the degree of photochemical oxidation (Wood et al., 2010) and aqueous-phase reaction (Ervens et al., 2011). In this study, we chose the relative number fractions of $^{43}C_2H_3O^+$, $^{89}HC_2O_4^-$, $^{62}NO_3^-$, $^{97}HSO_4^-$, and $^{18}NH_4^+$-containing particles to the total detected particles to indicate the secondary formation (Liang et al., 2022), respectively. The correlations between the number fraction of each secondary species with the oxidant concentrations ($O_x = O_3 + NO_2$) and RH are used to reflect the formation pathways during the two events (Chen et al., 2016).

As shown in Fig. 7, compared with E1 and E2, the linear relationships between the secondary aerosols and O_x are the opposite. During E1, $^{43}C_2H_3O^+$, $^{89}HC_2O_4^-$, $^{97}HSO_4^-$, $^{18}NH_4^+$ show significant negative linear correlation with O_x ($p < 0.01$), and the correlation strengths range from moderate to strong (r = –0.51 ~ –0.81), except that $^{62}NO_3^-$ fraction shows a certain higher but has no significant correlation with O_x (r = 0.33, $p > 0.05$). This might be influenced by the pollutant dispersion with the increased PBL height when O_x was evaluated (Fig. S9), offsetting the relatively low secondary formations (i.e., both precursors and local anthropogenic emissions are low) near the study location (Li et al., 2016). However, the number fraction of NO_3^- exhibits an upward trend with the increase of O_x concentration, due to the rise of NO_2 concentration (Fig. S9). During E1, the increase of NO_3^- could be generally ascribed to the local NO_2 emission, while the declines of other secondary components might be due to the reduced contribution of regional transportation to the other precursors. During E2, $^{43}C_2H_3O^+$ has less significant correlation with O_x (r = 0.37, $p > 0.05$), but with strong correlations with $^{89}HC_2O_4^-$, $^{97}HSO_4^-$, and $^{18}NH_4^+$ (r = 0.81~0.92, $p < 0.01$). It should be noted

https://doi.org/10.5194/acp-2022-786
Preprint. Discussion started: 16 December 2022

that $^{62}NO_3^-$ has a strong negative correlation (r =–0.85, p < 0.01) with O_x. These results suggest that photo-oxidation reactions have promoted secondary formation, among which the rate of HSO_4^- formation (slop = 0.017) is the highest. Increased with O_x concentration, the secondary organic species of $C_2H_3O^+$ (18%-28%) imperceptibly raise, and the oxalate also increases by 7%-20%. This result shows that the secondary organic species were different in the capacity of atmospheric oxidation formation, the obviously formed and accumulated secondary acids might be due to the formation of ammonium oxalate by adsorption of NH_3 gas (Sullivan et al., 2007; Nie et al., 2012; Kawamura and Bikkina, 2016; Lin et al., 2019). Increasing with O_x concentration, the relative fraction of NO_3^- decreases, attributed to its relatively volatile and difficult remote transport during the aging process, and the formation of organic nitrate. The previous study proves that the formations of organic nitrate species (such as $^{27}CHN^+$, $^{30}NO^+$, $^{43}CHO_1N^+$, and CHO_xN^+) through the NO+RO_2 pathway dominate 80% of the total nitrate in tropical forested regions during summertime (Alexander et al., 2009). Aruffo et al (2022) also found that low NO_x (e.g., < 6 ppb) (2.3±0.8 ppbv in this study) could even promote the particle-phase partitioning of the lower volatility of organonitrates.

Fig. 8 illustrates that $^{43}C_2H_3O^+$, $^{89}HC_2O_4^-$, $^{97}HSO_4^-$, and $^{18}NH_4^+$ have moderate to strong positive correlations with RH (r = 0.70~0.81, p < 0.01 or 0.05) during the two episode events, except that $^{43}C_2H_3O^+$ during E2 (p = 0.48) and $^{89}HC_2O_4^-$ during E1 (p = 0.12). Furthermore, $^{62}NO_3^-$ fraction also has no obvious changes and insignificant correlation with RH during E1 (p = 0.43) and presents a moderate negative correlation with RH (r = 0.69, p < 0.01) during E2. As shown in Fig. 8e, the aqueous formation rate of HSO_4^- is higher during the E1 (slop is 0.014) than in E2 (slop is 0.009) due to the low volatile and high hygroscopicity of sulfate (Wang et al., 2016; Zhang et al., 2019b; Sun et al., 2013). More favorable meteorological conditions during E1, including lower WS (0.08 ± 0.08 m s^{-1}) and temperature (3.9 ± 0.8°C), and higher RH (93.4 ± 7.6%), lead to the higher formation rate of HSO_4^- than that during E2 (with meteorological parameters of 2.4 ± 0.8 m s^{-1}, 6.9 ± 1.2°C, 60.7 ± 8.7%, respectively). The NH_4^+ species also have a greater production rate during the E1 (slop is 0.005) and E2 (slop is 0.006) due to the high RH. More abundant NH_3 precursors transported from the surrounding under the high WS and acidic anion fraction (i.e., sulfate, and oxalate) advance the NH_4^+ formation. Compared with those during E1, the secondary organic species (e.g.,

https://doi.org/10.5194/acp-2022-786
Preprint. Discussion started: 16 December 2022

$C_2H_3O^+$ and $HC_2O_4^-$) show inversed generation rates during E2. In addition, $C_2H_3O^+$ shows a strong correlation with RH (r = 0.70, $p < 0.05$) during E1 (slop is 0.003) but has insignificant correlation during E2. However, the $HC_2O_4^-$ fraction has a slight higher (9.7%-13.1%) during E1 and increases of correlation with RH (r = 0.81, $p < 0.01$) during E2 (slop is 0.003). These could be explained by the elevated ammonium oxalate and its precursor ((i.e.,$^{59}C_2H_3O_2^-$, $^{71}C_3H_3O_2^-$, $^{73}C_2HO_3^-$) concentrations from biomass burning (Ervens et al., 2011; Li et al., 2022b). The linearity between $^{62}NO_3^-$ and RH (r = 0.69, $p < 0.01$) decreases during E2, mostly due to the low NO_2 concentration (2.6 ± 0.7 ppb) which further decreases with elevating O_3 (Fig. S10). Meanwhile, high RH could promote organonitrates formation (Fang et al., 2021; Fry et al., 2014). No obvious change and insignificant correlation between NO_3^- and RH during E1, potentially attributed to the decreases of NO_2 concentration (3.7 ± 0.4 ppb) in the local atmosphere.

4 Conclusions

This study presents the chemical composition, size distribution, mixing state, and secondary formation of individual particles in the southeastern margin of TP, China during the pre-monsoon season using a high-resolution SPAMS. The finding shows that the rich-K (30.9%) and BB types (18.7%) are the two dominant aerosol particles in the remote area; followed by the OC (12.8%), Ammonium (11.9%), EC-aged (10.9%), and Dust (10.7%) types; the NaK-SN, Metal and Others types contributed 0.3–2.8% to the total amibent particles. By interpreting the mass spectra and diurnal trends, the major particle types are mainly from traffic emission, biomass burning, secondary formation, and fly ash, while the dynamics of the PBL height could also affect the contributions of these particles. The observed change in the number fraction of the particle types was mainly influenced by air masses (97.61% of the total trajectories) from northeastern Myanmar, and significantly contributed to rich-K and BB types. The particle types show distinct size distributions. The two most critical particle types of rich-K and BB appear in a unimodal pattern, the fractions of OC and EC-aged gradually decrease with the increase of the particle sizes, but Ammonium and Dust types show the opposite. Sulfate is the major secondary species and is highly mixed with rich-K, Ammonium, and EC-aged types. Nitrate has a relatively low mixing ratio due to its higher volatility than sulfate during regional transportation, except for BB and OC types. During the entire study

https://doi.org/10.5194/acp-2022-786
Preprint. Discussion started: 16 December 2022

campaign, two air episodes with the high number concentration particle occurred but with significant differences in each particle fraction due to the different meteorological conditions (RH, WS, etc.). The results of the formation mechanism of secondary species demonstrate that the formation capacity of atmospheric oxidation is affected by the PBL height, but the relative humidity (RH) could promote the formation of secondary species, especially $^{97}HSO_4^-$ and $^{18}NH_4^+$. The results of this study provide useful information concerning the detailed characteristic of aerosol components, size distribution, and mixing states in the southeast TP, and highlight the importance of the cross-border transport and formation mechanism of aerosols in high-altitude regions.

Data availability. The data presented in this study are available at the Zenodo data archive https://doi.org/10.5281/zenodo.7336857.

Competing interests. The authors declare that they have no conflict of interest.

Author contributions. QW and JC designed the campaign. WR conducted field measurements. LL, QW, JT, and YZ made data analysis and interpretation. LL and QW wrote the paper. All the authors reviewed and commented on the paper.

Acknowledgments. The authors are grateful to the staff from Lijiang Astronomical Station for their assistance with field sampling. The authors are also grateful to Weikang Ran, Yonggang Zhang, and other staff for the field observation.

Financial support. This work was supported by the National Natural Science Foundation of China (41877391), the Second Tibetan Plateau Scientific Expedition and Research Program (STEP) (2019QZKK0602), and the Youth Innovation Promotion Association of the Chinese Academy of Sciences (2019402).

Reference

Alexander, B., Hastings, M. G., Allman, D. J., Dachs, J., Thornton, J. A., and Kunasek, S. A.: Quantifying atmospheric nitrate formation pathways based on a global model of the oxygen isotopic composition ($\Delta^{17}O$) of atmospheric nitrate, Atmos. Chem. Phys., 9, 5043–5056, https://doi.org/10.5194/acp-9-5043-2009, 2009.

Angelino, S., Suess, D. T., and Prather, K. A.: Formation of aerosol particles from reactions of secondary and tertiary alkylamines: characterization by aerosol time-of-flight mass spectrometry, Environ. Sci. Technol., 35, 3130–3138, https://doi.org/10.1021/es0015444, 2001.

Aruffo, E., Wang, J., Ye, J., Ohno, P., Qin, Y., Stewart, M., McKinney, K., Di Carlo, P., and Martin, S. T.: Partitioning of Organonitrates in the Production of Secondary Organic Aerosols from α-Pinene Photo-Oxidation, Environ. Sci. Technol., 56, 5421–5429, https://doi.org/10.1021/acs.est.1c08380, 2022.

Bi, X. H., Zhang, G. H., Li, L., Wang, X. M., Li, M., Sheng, G. Y., Fu, J. M., and Zhou, Z.: Mixing state of biomass burning particles by single particle aerosol mass spectrometer in the urban area of PRD, China, Atmos. Environ., 45, 3447–3453, https://doi.org/10.1016/j.atmosenv.2011.03.034, 2011.

Bi, X. H., Lin, Q. H., Peng, L., Zhang, G. H., Wang, X. M., Brechtel, F. J., Chen, D. H., Li, M., Peng, P. A., Sheng, G. Y., and Zhou, Z.: In situ detection of the chemistry of individual fog droplet residues in the

Pearl River Delta region, China, J. Geophys. Res. Atmos., 121, 9105–9116, https://doi.org/10.1002/2016jd024886, 2016.

Budisulistiorini, S. H., Riva, M., Williams, M., Chen, J., Itoh, M., Surratt, J. D., and Kuwata, M.: Light-absorbing brown carbon aerosol constituents from combustion of Indonesian peat and biomass, Environ. Sci. Technol., 51, 4415-4423, https://doi.org/10.1021/acs.est.7b00397, 2017.

Canagaratna, M. R., Jayne, J. T., Jimenez, J. L., Allan, J. D., Alfarra, M. R., Zhang, Q., Onasch, T. B., Drewnick, F., Coe, H., Middlebrook, A., Delia, A., Williams, L. R., Trimborn, A. M., Northway, M. J., DeCarlo, P. F., Kolb, C. E., Davidovits, P., and Worsnop, D. R.: Chemical and microphysical characterization of ambient aerosols with the aerodyne aerosol mass spectrometer, Mass Spectrom. Rev., 26, 185–222, https://dx.doi.org/10.1002/mas.20115, 2007.

Cao, J. J., Tie X. X., Xu B., Zhao, Z. Z., Zhu, C. S., Li, G. H., and Liu, S. X.: Measuring and modelling black carbon (BC) contamination in the SE Tibetan Plateau, J. Atmos. Chem., 67, 45–60, https://doi.org/10.1007/s10874-011-9202-5, 2010.

Chan, C. Y., Wong, K. H., Li, Y. S., Chan, Y., and Zhang, X.D.: The effects of Southeast Asia fire activities on tropospheric ozone, trace gases and aerosols at a remote site over the Tibetan Plateau of Southwest China, Tellus B, 58B, 310–318, https://doi.org/10.1111/j.1600-0889.2006.00187.x, 2017.

Chen, P. F., Shichang Kang, S. C., Bai, J. K., Sillanpää, M., and Li, C. L.: Yak dung combustion aerosols in the Tibetan Plateau: Chemical characteristics and influence on the local atmospheric environment, Atmos. Res., 156, 58–66, https://doi.org/10.1016/j.atmosres.2015.01.001, 2015.

Chen, Y., Cao, J. J., Huang, R. J., Yang, F. M., Wang, Q. Y., and Wang, Y. C.: Characterization, mixing state, and evolution of urban single particles in Xi'an (China) during wintertime haze days, Sci. Total Environ., 573, 937–945, https://doi.org/10.1016/j.scitotenv.2016.08.151, 2016.

Chen, Y., Wenger, J. C., Yang, F. M., Cao, J. J., Huang, R. J., Shi, G. M., Zhang, S. M., Tian, M., and Wang, H. B.: Source characterization of urban particles from meat smoking activities in Chongqing, China using single particle aerosol mass spectrometry, Environ. Pollut., 228, 92–101, https://doi.org/10.1016/j.envpol.2017.05.022, 2017.

Chen, Y., Tian, M., Huang, R. J., Shi, G. M., Wang, H. B., Peng, C., Cao, J. J., Wang, Q. Y., Zhang, S. M., Guo, D. M., Zhang, L. M., and Yang, F. M.: Characterization of urban amine-containing particles in southwestern China: seasonal variation, source, and processing, Atmos. Chem. Phys., 19, 3245–3255, https://doi.org/10.5194/acp-19-3245-2019, 2019.

Chen, J. Q., and Bordoni, S.: Orographic effects of the Tibetan Plateau on the East Asian Summer Monsoon: An energetic perspective, J. Climate., 27, 3052–3072, https://doi.org/10.1175/JCLI-D-13-00479.1, 2014.

Crippa, M., DeCarlo, P. F., Slowik, J. G., Mohr, C., Heringa, M. F., Chirico, R., Poulain, L., Freutel, F., Sciare, J., Cozic, J., Di Marco, C. F., Elsasser, M., Nicolas, J. B., Marchand, N., Abidi, E., Wiedensohler, A., Drewnick, F., Schneider, J., Borrmann, S., Nemitz, E., Zimmermann, R., Jaffrezo, J. L., Prévôt, A. S. H., and Baltensperger, U.: Wintertime aerosol chemical composition and source apportionment of the organic fraction in the metropolitan area of Paris, Atmos. Chem. Phys., 13, 961–981, https://doi.org/10.5194/acp-13-961-2013, 2013.

Dall'Osto, M., Beddows, D.C.S., Gietl, J. K., Olatunbosun, O. A., Yang, X. G., and Harrison, R. M.: Characteristics of tyre dust in polluted air: studies by single particle mass spectrometry (ATOFMS), Atmos. Environ. 94, 224–230, https://doi.org/10.1016/j.atmosenv.2014.05.026, 2014.

Dall'Osto, M., and Harrison, R. M.: Urban organic aerosols measured by single particle mass spectrometry in the megacity of London, Atmos. Chem. Phys., 12, 4127–4142,

http://dx.doi.org/10.5194/acp-12-4127–2012, 2012.

Du, W., Sun, Y. L., Xu, Y. S., Jiang, Q., Wang, Q. Q., Wang, W., Wang, F., Bai, Z. P., Zhao, X. D., and Yang, Y. C.: Chemical characterization of submicron aerosol and particle growth events at a national background site (3295 m a.s.l.) on the Tibetan Plateau, Atmos. Chem. Phys., 15, 10811–10824, https://doi.org/10.5194/acp-15-10811-2015, 2015.

Dusek, U., Frank, G. P., Hildebrandt, L., Curtius, J., Schneider, J., Walter, S., Chand, D., Drewnick, F., Hings, S., Jung, D., Borrmann, S., and Andreae, M. O.: Size matters more than chemistry for cloud-nucleating ability of aerosol particles, Science, 312, 1375–1378, https://doi.org/10.1126/science.1125261, 2006.

Engling, G., Zhang, Y. N., Chan, C. Y., Sang, X. F., Lin, M., Ho, K. F., Li, Y. S., Lin, C. Y., and Lee, J. J.: Characterization and sources of aerosol particles over the southeastern Ti-betan Plateau during the Southeast Asia biomass-burning season, Tellus B, 63, 117–128, https://doi.org/10.1111/j.1600-0889.2010.00512.x, 2011.

Ervens, B., Turpin, B. J., and Weber, R. J.: Secondary organic aerosol formation in cloud droplets and aqueous particles (aqSOA): a review of laboratory, feld and model studies, Atmos. Chem. Phys., 11, 11069–11102, https://doi.org/10.5194/acp-11-11069-2011, 2011.

Fang, X. Z., Liu, Y. Y., Li, K. J., Wang, T., Deng, Y., Feng, Y. Q., Yang, Y., Cheng, H. Y., Chen, J. M., and Zhang, L. W.: Atmospheric Nitrate Formation through Oxidation by Carbonate Radical, ACS Earth Space Chem., 5, 1801–1811, https://doi.org/10.1021/acsearthspacechem.1c00169, 2021.

Fry, J. L., Draper, D. C., Barsanti, K. C., Smith, J. N., Ortega, J., Winkler, P. M., Lawler, M. J., Brown, S. S., Edwards, P. M., Cohen, R. C., and Lee, L.: Secondary Organic Aerosol Formation and Organic Nitrate Yield from NO_3 Oxidation of Biogenic Hydrocarbons, Environ. Sci. Technol., 48, 11944–11953, https://doi.org/10.1021/es502204x, 2014.

Gettelman, A., Morrison, H., Terai, C. R., and Wood, R.: Microphysical process rates and global aerosolecloud interactions, Atmos. Chem. Phys., 13, 9855–9867, https://doi.org/10.5194/acp-14-9099-2014, 2013.

Han, H., Wu, Y., Liu, J., Zhao, T. L., Zhuang, B. L., Wang, H. L., Li, Y. C., Chen, H. M., Zhu, Y., Liu, H. N., Wang, Q. G., Li, S., Wang, T. J., Xie, M., and Li, M. M.: Impacts of atmospheric transport and biomass burning on the inter-annual variation in black carbon aerosols over the Tibetan Plateau, Atmos. Chem. Phys., 20, 13591–13610, https://doi.org/10.5194/acp-20-13591-2020, 2020.

Hua, S., Liu, Y. Z., Luo, R., Shao, T. B., Zhu, Q. Z.: Inconsistent aerosol indirect effects on water clouds and ice clouds over the Tibetan Plateau, Int. J. Climatol., 40, 3832–3848, https://doi.org/10.1002/joc.6430, 2019.

Immerzeel, W. W., van Beek, L. P. H., and Bierkens, M. F. P.: Climate change will affect the Asian water towers, Science, 328, 1382–1385, https://doi.org/10.1126/science.1183188, 2010.

Jacobson, M. Z.: Analysis of aerosol interactions with numerical techniques for solving coagulation, nucleation, condensation, dissolution, and reversible chemistry among multiple size distributions, J. Geophys. Res., 107(D19), 4366, https://doi.org/10.1029/2001JD002044, 2002.

Jiang, H. H., Frie, A. L., Lavi, A., Chen, J. Y., Zhang, H., Bahreini, R., and Lin, Y. H.: Brown carbon formation from nighttime chemistry of unsaturated heterocyclic volatile organic compounds, Environ. Sci. Technol. Lett., 6, 184190, https://doi.org/10.1021/acs.estlett.9b00017, 2019.

Kawamura, K. and Bikkina, S.: A review of dicarboxylic acids and related compounds in atmospheric aerosols: molecular distributions, sources and transformation, Atmos. Res., 170, 140–160, https://doi.org/10.1016/j.atmosres.2015.11.018, 2016.

https://doi.org/10.5194/acp-2022-786
Preprint. Discussion started: 16 December 2022

Kumar, M., Raju, M. P., Singh, R. K., Singh, A. K., Singh, R. S., and Banerjee, T.: Wintertime characteristics of aerosols over middle Indo-Gangetic Plain: vertical profile, transport and radiative forcing, Atmos. Res., 183, 268–282, https://doi.org/10.1016/j.atmosres.2016.09.012, 2017.

Lian, X. F., Zhang, G. H., Yang, Y. X., Lin, Q. H., Fu, Y. Z., Jiang, F., Peng, L., Hu, X. D., Chen, D. H., Wang, X. M., Peng, P. A., Sheng, G. Y., and Bi, X. H.: Evidence for the Formation of Imidazole from Carbonyls and Reduced Nitrogen Species at the Individual Particle Level in the Ambient Atmosphere, Environ. Sci. Technol. Lett., 8, 9–15. https://dx.doi.org/10.1021/acs.estlett.0c00722, 2021.

Liang, Z. C., Zhou, L. Y., Cuevas, R. A., Li, X. Y., Cheng,C. L., Li, M., Tang, R. Z., Zhang, R. F., Lee Patrick K. H., Lai, Alvin C. K., and Chan, C.K.: Sulfate Formation in Incense Burning Particles: A Single-Particle Mass Spectrometric Study, Environ. Sci. Technol. Lett., 9, 718–725, https://doi.org/10.1021/acs.estlett.2c00492, 2022.

Li, C. L., Bosch, C., Kang, S. C., Andersson, A., Chen, P. F., Zhang, Q. G., Cong, Z. Y., Chen, B., Qin, D. H., and Gustafsson., Ö.: Sources of black carbon to the Himalayan–Tibetan Plateau glaciers, Nat. Commun., 7, 12574, https://doi.org/10.1038/ncomms12574, 2016b.

Li, C. L., Bosch, C., Kang, S. C., Andersson, A., Chen, P. F., Zhang, Q. G., Cong, Z. Y., Tripathee, L., and Örjanb, G.: ^{14}C characteristics of organic carbon in the atmosphere and at glacier region of the Tibetan Plateau, Sci. Total Environ., 832, 155020, https://doi.org/10.1016/j.scitotenv.2022.155020, 2022a.

Li, L., Huang, Z. X., Dong, J. G., Li, M., Gao, W., Nian, H. Q., Fu, Z., Zhang, G. H., Bi, X. H., Cheng, P., and Zhou, Z.: Real time bipolar time-of-flight mass spectrometer for analyzing single aerosol particles, Int. J. Mass Spectrom., 303, 118–124, https://doi.org/10.1016/j.ijms.2011.01.017, 2011.

Li, L., Li, M., Huang, Z. X., Gao, W., Nian, H. Q., Fu, Z., Gao, J., Chai, F. H., and Zhou, Z.: Ambient particle characterization by single particle aerosol mass spectrometry in an urban area of Beijing, Atmos. Environ., 94, 323–331, https://doi.org/10.1016/j.atmosenv.2014.03.048, 2014.

Li L., Wang, Q. Y., Zhang, Y., Liu, S. X., Zhang, T., Wang, S., Tian, J., Chen, Y., Hang Ho, S. S., Han, Y., and Cao, J.J.: Impact of reduced anthropogenic emissions on chemical characteristics of urban aerosol by individual particle analysis, Chemosphere, 303, 135013, https://doi.org/10.1016/j.chemosphere.2022.135013, 2022b.

Li, J. J., Wang, G. H., Wang, X. M., Cao, J. J., Sun, T., Cheng, C. L., Meng, J. J., Hu, T. F., and Liu, S. X.: Abundance, composition and source of atmospheric $PM_{2.5}$ at a remote site in the Tibetan Plateau, China, Tellus B, 65, http://dx.doi.org/10.3402/tellusb.v65i0.20281, 2013.

Li, Y. J., Sun, Y. L., Zhang, Q., Li, X., Li, M., Zhou, Z., and Chan, C. K.: Real-time chemical characterization of atmospheric particulate matter in China: A review, Atmos. Environ., 158, 270–304, http://dx.doi.org/10.1016/j.atmosenv.2017.02.027, 2017.

Lin, Q. H., Bi, X. H., Zhang, G. H., Yang, Y. X., Peng, L., Lian, X. F., Fu, Y. Z., Li, M., Chen, D. H., Miller, M., Ou, J., Tang, M. J., Wang, X. M., Peng, P. A., Sheng, G. Y., and Zhou, Z.: In-cloud formation of secondary species in iron-containing particles, Atmos. Chem. Phys., 19, 1195–1206, https://doi.org/10.5194/acp-19-1195-2019, 2019

Link, M. F., Kim, J., Park, G., Lee, T., Park, T., Babar, Z. B., Sung, K., Kim, P., Kang, S., Kim, J. S., Choi, Y., Son, J., Lim, H. J., and Farmer, D.K.: Elevated production of NH_4NO_3 from the photochemical processing of vehicle exhaust: Implications for air quality in the Seoul Metropolitan Region, Atmos. Environ., 156, 95–101, https://doi.org/10.1016/j.atmosenv.2017.02.031, 2017.

Liu, Y. Z., Zhu, Q. Z., Huang, J. P., Hua, S., and Jia, R.: Impact of dust-polluted convective clouds over the Tibetan Plateau on downstream precipitation, Atmos. Environ., 209, 67–77, https://doi.org/10.1016/j.atmosenv.2019.04.001, 2019.

Liu, Q., Liu, D. T., Gao, Q., Tian, P., Wang, F., Zhao, D. L., Bi, K., Wu, Y. Z., Ding, S., Hu, K., Zhang, J. L., Ding, D. P., Zhao, C. S.: Vertical characteristics of aerosol hygroscopicity and impacts on optical properties over the North China Plain during winter, Atmos. Chem. Phys., 20, 3931–3944, https://doi.org/10.5194/acp-20-3931-2020, 2020a.

Liu, D. T., Hu, K., Zhao, D. L., Ding, S., Wu, Y. F., Zhou, C., Yu, C. J., Tian, P., Liu, Q., Bi, K., Wu, Y. Z., Hu, B., Ji, D. S., Kong, S. F., Ouyang, B., He, H., Huang, M. Y., and Ding, D.P.: Efficient Vertical Transport of Black Carbon in the Planetary Boundary Layer, Geo. Res. Lett., 47, 1–10, https://doi.org/10.1029/2020GL088858, 2020b

Liu, H. K., Wang, Q. Y., Xing, L., Zhang, Y., Zhang, T., Ran, W. K., Cao, J. J.: Measurement report: quantifying source contribution of fossil fuels and biomass-burning black carbon aerosol in the southeastern margin of the Tibetan Plateau, Atmos. Chem. Phys., 21, 973–987, https://doi.org/10.5194/acp-21-973-2021, 2021.

Luo, M., Liu, Y. Z., Zhu, Q. Z., Tang, Y. H., and Alam, K.: Role and mechanisms of black carbon affecting water vapor transport to Tibet, Remote Sens., 12, 231, https://doi.org/10.3390/rs12020231, 2020.

Ma, L., Li, M., Huang, Z. X., Li, L., Gao, W., Nian, H. Q., Zou, L. L., Fu, Z., Gao, J., Chai, F. H., and Zhou, Z.: Real time analysis of lead-containing atmospheric particles in Beijing during springtime by single particle aerosol mass spectrometry, Chemosphere, 154, 454–462, https://doi.org/10.1016/j.chemosphere.2016.04.001, 2016.

Ma, X., Yu, F., and Luo, G.: Aerosol direct radiative forcing based on GEOS-Chem-APM and uncertainties, Atmos. Chem. Phys., 12, 5563–5581, https://doi.org/10.5194/acp-12-5563-2012, 2012.

Mahowald, N. M., Albani, S., Kok, J. F., Engelstaedter, S., Scanza, R., Ward, D. S., and Flanner, M. G.: The size distribution of desert dust aerosols and its impact on the Earth system, Aeolian Res., 15, 53–71, https://doi.org/10.1016/j.aeolia.2013.09.002, 2014.

Matsui, H.: Black carbon simulations using a size- and mixingstate-resolved three-dimensional model: 2. Aging timescale and its impact over East Asia, J. Geophys. Res.-Atmos., 121, 1808–1821, https://doi.org/10.1002/2015jd023999, 2016.

McFiggans, G., Artaxo, P., Baltensperger, U., Coe, H., Facchini, M.C., Feingold, G., Fuzzi, S., Gysel, M., Laaksonen, A., Lohmann, U., Mentel, T. F., Murphy, D. M., O'Dowd, C. D., Snider, J.R., and Weingartner, E.: The effect of physical and chemical aerosol properties on warm cloud droplet activation, Atmos. Chem. Phys., 6, 2593–2649, https://doi.org/10.5194/acp-6-2593-2006, 2006.

Moffet, R. C., Foy, B. D., Molina, L. A., Molina, M. J., and Prather, K. A.: Measurement of ambient aerosols in northern Mexico City by single particle mass spectrometry, Atmos. Chem. Phys., 8 (16), 4499–4516, https://doi.org/10.5194/acpd-7-6413-2007, 2008.

Ng, N. L., Canagaratna, M. R., Jimenez, J. L., Chhabra, P. S., Seinfeld, J. H., and Worsnop, D. R.: Changes in organic aerosol composition with aging inferred from aerosol mass spectra, Atmos. Chem. Phys., 11(13), 6465-6474, https://doi.org/10.5194/acp-11-6465-2011, 2011.

Nie, W., Wang, T., Xue, L. K., and Ding, A. J.: Asian dust storm observed at a rural mountain site in southern china: chemical evolution and heterogeneous photochemistry, Atmos. Chem. Phys., 12, 11985–11995, https://doi.org/10.5194/acp-12-11985-2012, 2012.

Pratt, K. A., Hatch, L. E., and Prather, K. A.: Seasonal volatility dependence of ambient particle phase amines, Environ. Sci. Technol., 43, 5276–5281, https://doi.org/10.1021/es803189n, 2009.

Pratt, K. A., Murphy, S. M., Subramanian, R., DeMott, P. J., Kok, G. L., Campos, T., Rogers, D. C., Prenni, A. J., Heymsfield, A. J., Seinfeld, J. H., and Prather, K. A.: Flight-based chemical characterization of biomass burning aerosols within two prescribed burn smoke plumes, Atmos. Chem. Phys., 11,

12549–12565, https://doi.org/10.5194/acp-11-12549-2011, 2011.

Pratt, K.A. and Prather, K.A.: Aircraft measurements of vertical profiles of aerosol mixing states, J. Geophys. Res., 115, D11305, https://doi.org/10.1029/2009jd013150, 2010.

Prather, P.A., Nordmeyer, T., and Salt, K.: Real-time characterization of individual aerosol particles using time-of-flight mass spectrometry, Anal. Chem., 66, 1403–1407, https://dx.doi.org/10.1021/ac00081a007, 1994.

Qian, Y., Flanner, M. G., Leung, L. R., and Wang, W.: Sensitivity studies on the impacts of Tibetan Plateau snowpack pollution on the Asian hydrological cycle and monsoon climate, Atmos. Chem. Phys., 11, 1929-1948, https://doi.org/10.5194/acp-11-1929-2011, 2011.

Rehbein, P. J., Jeong, C. H., McGuire, M. L., Yao, X., Corbin, J. C., and Evans, G. J.: Cloud and fog processing enhanced gas-toparticle partitioning of trimethylamine, Environ. Sci. Technol., 45, 4346–4352, https://doi.org/10.1021/es1042113, 2011.

Robinson, A. L., Donahue, N. M., Shrivastava, M. K., Weitkamp, E. A., Sage, A. M., Grieshop, A. P., Lane, T. E., Pierce, J. R., and Pandis, S.N.: Rethinking organic aerosols: Semivolatile emissions and photochemical aging, Science, 315, 1259–1262, https://doi.org/10.1126/science.1133061, 2007.

Roth, A., Schneider, J., Klimach, T., Mertes, S., van Pinxteren, D., Herrmann, H., and Borrmann, S.: Aerosol properties, source identification, and cloud processing in orographic clouds measured by single particle mass spectrometry on a central European mountain site during HCCT-2010, Atmos. Chem. Phys., 16, 505–524, https://doi.org/10.5194/acp-16-505-2016, 2016.

Seinfeld, J. H., and Pandis, S. N.: Atmospheric Chemistry and Physics: from Air Pollution to Climate Change, John Wiley & Sons., 1326. https://doi.org/10.1080/00139157.1999.10544295, 2012.

Shen, L. J., Wang, H. L., Yin, Y., Chen, J. H., and Chen, K.: Observation of atmospheric new particle growth events at the summit of mountain Tai (1534 m) in Central East China, Atmos. Environ., 201, 148–157, https://doi.org/10.1016/j.atmosenv.2018.12.051, 2019.

Shen, L. J., Wang, H. L., Lü, S., Zhang, X. H., Yuan, J., Tao, S. K., Zhang, G. J., Wang, F., and Li, L.: Influence of pollution control on air pollutants and the mixing state of aerosol particles during the 2nd World Internet Conference in Jiaxing, China, J. Clean. Prod., 149, 436–447, https://doi.org/10.1016/j.jclepro.2017.02.114, 2017.

Shen, R. Q., Ding, X., He, Q. F., Cong, Z. Y., Yu, Q. Q., and Wang, X. M.: Seasonal variation of secondary organic aerosol tracers in Central Tibetan Plateau, Atmos. Chem. Phys., 15, 8781-8793, https://doi.org/10.5194/acp-15-8781-2015, 2015.

Sirois, A. and Bottenheim, J. W.: Use of backward trajectories to interpret the 5-year record of PAN and O3 ambient air concentrations at Kejimkujik National Park, Nova Scotia, J. Geophys. Res., 100, 2867–2881, https://doi.org/10.1029/94JD02951, 1995.

Song, X. H., and Hopke, P. K.: Classifcation of single particles analyzed by ATOFMS using an artifcial neural network, ART-2A, Anal. Chem., 71, 860–865, https://doi.org/10.1021/ac9809682, 1999.

Sorooshian, A., Lu, M. L., Brechtel, F. J., Jonsson, H., Feingold, G., Flagan, R. C., and Seinfeld, J. H.: On the source of organic acid aerosol layers above clouds, Environ. Sci. Technol., 41, 4647–4654, https://doi.org/10.1021/es0630442, 2007.

Sullivan, R. C., Guazzotti, S. A., Sodeman, D. A., and Prather, K. A.: Direct observations of the atmospheric processing of Asian mineral dust, Atmos. Chem. Phys., 7, 1213–1236, https://doi.org/10.5194/acp-7-1213-2007, 2007.

Sun, Y. L, Wang, Z. F., Fu, P. Q., Jiang, Q. J., Yang, T., Li, J., and Ge, X. L.: The impact of relative humidity on aerosol composition and evolution processes during wintertime in Beijing, China, Atmos.

Environ., 77, 927–934, https://doi.org/10.1016/j.atmosenv.2013.06.019, 2013.

Volkamer, R., Jimenez, J. L., San Martini, F., Dzepina, K., Zhang, Q., Salcedo, D., Molina, L. T., Worsnop, D. R., and Molina, M. J.: Secondary organic aerosol formation from anthropogenic air pollution: rapid and higher than expected, Geophys. Res. Lett., 33 (17), https://doi.org/10.1029/2006GL026899, 2006.

Wang, A. Q., Xie, X. N., Liu, X. D., and Yin, Z. Y.: Direct Radiative Effect (DRE) of Dust Aerosols on West African and East Asian Monsoon: The Role of Ocean-Atmosphere Interactions, J. Geophys. Res.Atmos., 127, 1–20, https://doi.org/10.1029/2021JD035917, 2022.

Wang, G. H., Zhang, R. Y., Gomez, M. E., Yang, L. X., Zamora, M. L., Hu, M., Lin, Y., Peng, J. F., Guo, S., Meng, J. J., Li, J. J., Cheng, C. L., Hu, T. F., Ren, Y. Q., Wang, Y. S., Gao, J., Cao, J. J., An, Z. S., Zhou, W. J., Li, G. H., Wang, J. Y., Tian, P. F., Marrero-Ortiz, W., Secrest, J., Du, Z. F., Zheng, J., Shang, D. J., Zeng, L. M., Shao, M., Wang, W. G., Huang, Y., Wang, Y., Zhu, Y. J., Li, Y. X., Hu, J. X., Pan, B. W., Cai, L., Cheng, Y. T., Ji, Y. M., Zhang, Y., Rosenfeld, D., Liss, P. S., Duce, R. A., Kolb, C. E., and Molina., M. J.: Persistent sulfate formation from London Fog to Chinese haze, P. Natl. Acad. Sci. USA, 113(48), 13630–13635, https://doi.org/10.1073/pnas.1616540113, 2016.

Wang, H. L., An, J. L., Shen, L. J., Zhu, B., Xia, L., Duan, Q., and Zou, J. N.: Mixing state of ambient aerosols in Nanjing city by single particle mass spectrometry, Atmos. Environ., 132, 123–132, https://dx.doi.org/10.1016/j.atmosenv.2016.02.032, 2016.

Wang, H. L., Shen, L. J., Yin, Y., Chen, K., Chen, J. H., and Wang, Y. S.: Characteristics and mixing state of aerosol at the summit of Mount Tai (1534 m) in Central East China: First measurements with SPAMS, Atmos. Environ., 213, 273–284, https://doi.org/10.1016/j.atmosenv.2019.06.021, 2019b.

Wang, Q. Y., Han, Y. M., Ye, J. H., Liu, S. X., Pongpiachan, S., Zhang, N. N., Han, Y. M., Tian, J., Wu, C., Long, X., Zhang, Q., Zhang, W. Y., Zhao, Z. Z., and Cao, J. J.: High contribution of secondary brown carbon to aerosol light absorption in the southeastern margin of Tibetan Plateau, Geophys. Res. Lett., 46, 4962–4970, https://doi.org/10.1029/2019GL082731, 2019a.

Wang, Q. Y., Cao, J. J., Han, Y. M., Tian, J., Zhu, C. S., Zhang, Y., Zhang, N. N., Shen, Z. X., Ni, H. Y., Zhao, S. Y., and Wu, J. R.: Sources and physicochemical characteristics of black carbon aerosol from the southeastern Tibetan Plateau: internal mixing enhances light absorption, Atmos. Chem. Phys., 18, 4639–4656, https://doi.org/10.5194/acp-18-4639-2018, 2018.

William, K.M.L., Maeng-Ki, K., Kyu-Myong, K., and Woo-Seop, L.: Enhanced surface warming and accelerated snow melt in the Himalayas and Tibetan Plateau induced by absorbing aerosols, Environ. Res. Lett., 5(2), 025204, https://doi.org/10.1088/1748-9326/5/2/025204, 2010.

Wood, E. C., Canagaratna, M. R., Herndon, S. C., Onasch, T. B., Kolb, C. E., Worsnop, D. R., Kroll, J. H., Knighton, W. B., Seila, R., Zavala, M., Molina, L. T., DeCarlo, P. F., Jimenez, J. L., Weinheimer, A. J., Knapp, D. J., Jobson, B. T., Stutz, J., Kuster, W. C., and Williams, E. J.: Investigation of the correlation between odd oxygen and secondary organic aerosol in Mexico City and Houston, Atmos. Chem. Phys., 10, 8947–8968, https://doi.org/10.5194/acp-10-8947-2010, 2010.

Xia, X., Chen, H., Goloub, P., Zhang, W., Chatenet, B., and Wang, P.: A compilation of aerosol optical properties and calculation of direct radiative forcing over an urban region in northern China, J. Geophys. Res., 112, D12203, https://doi.org/10.1029/2006jd008119, 2007.

Xu, L. L., Wu, X., Hong, Z. Y., Zhang, Y. R., Deng, J. J., Hong, Y. W., and Chen, J. S.: Composition, mixing state, and size distribution of single submicron particles during pollution episodes in a coastal city in southeast China, Environ. Sci. Pollut. Res., 26, 1464–1473, https://doi.org/10.1007/s11356-018-3469-x, 2018.

Xu, W. Q., Han, T. T., Du, W., Wang, Q. Q., Chen, C., Zhao, J., Zhang, Y. J., Li, J., Fu, P. Q., Wang, Z. F.,

Worsnop, D. R., and Sun, Y. L.: Effects of aqueous-phase and photochemical processing on secondary organic aerosol formation and evolution in Beijing, China, Environ. Sci. Technol., 51, 762−770, https://doi.org/10.1021/acs.est.6b04498, 2017.

Xue, J., Griffth, S. M., Yu, X., Lau, A.K.H., and Yu, J. Z.: Effect of nitrate and sulfate relative abundance in $PM_{2.5}$ on liquid water content explored through half-hourly observations of inorganic soluble aerosols at a polluted receptor site, Atmos. Environ., 99, 24–31, https://doi.org/10.1016/j.atmosenv.2014.09.049, 2014.

Yang, J., Ma, S. X., Gao, B., Li, X. Y., Zhang, Y. J., Cai, J., Li, M., Yao, L. A., Huang, B., and Zheng, M.: Single particle mass spectral signatures from vehicle exhaust particles and the source apportionment of on-line $PM_{2.5}$ by single particle aerosol mass spectrometry, Sci. Total Environ., 593, 310–318, https://doi.org/10.1016/j.scitotenv.2017.03.099, 2017.

Yao, T. D., Thompson, L. G., Mosbrugger, V., Zhang, F., Ma, Y. M., Luo, T. X., Xu, B. Q., Yang, X. X., Joswiak, D. R., Wang, W. C., Joswiak, M. E., Devkota, L. P., Tayal, S., Jilani, R., and Fayziev, R.: Third Pole Environment (TPE), Environ. Dev., 3, 52-64, http://doi.org/10.1016/j.envdev.2012.04.002, 2012.

Zaveri, R. A., Barnard, J., Easter, R., Riemer, N., and West, M.: Particle-resolved simulation of aerosol size, composition, mixing state, and the associated optical and cloud condensation nuclei activation properties in an evolving urban plume, J. Geophys. Res., 115, D17210, https://doi.org/10.1029/2009JD013616, 2010.

Zhang, G. H., Bi, X. H., Chan, L. Y., Li, L., Wang, X. M., Feng, J. L., Sheng, G. Y., Fu, J. M., Li, M., and Zhou, Z.: Enhanced trimethylamine-containing particles during fog events detected by single particle aerosol mass spectrometry in urban Guangzhou, China, Atmos. Environ., 55, 121–126, https://doi.org/10.1016/j.atmosenv.2012.03.038, 2012.

Zhang, G. H., Han, B. X., Bi, X. H., Dai, S. X., Huang, W., Chen, D. H., Wang, X. M., Sheng, G. Y., Fu, J. M., and Zhou, Z.: Characteristics of individual particles in the atmosphere of Guangzhou by single particle mass spectrometry, Atmos. Res., 153, 286–295, https://doi.org/10.1016/j.atmosres.2014.08.016, 2015.

Zhang, J. K., Luo, B., Zhang, J. Q., Ouyang, F., Song, H. Y., Liu, P. C., Cao, P., Schäfer, K., Wang, S. G., Huang, X. J., and Lin, Y. F.: Analysis of the characteristics of single atmospheric particles in Chengdu using single particle mass spectrometry, Atmos. Environ., 157, 91–100, https://doi.org/10.1016/j.atmosenv.2017.03.012, 2017.

Zhang, G. H., Han, B. X., Bi, X. H., Dai, S. X., Huang, W., Chen, D. H., Wang, X. M., Sheng, G. Y., Fu, J. M., and Zhou, Z.: Characteristics of individual particles in the atmosphere of Guangzhou by single particle mass spectrometry, Atmos. Res., 153, 286–295, https://dx.doi.org/10.1016/j.atmosres.2014.08.016, 2015.

Zhang, J. K., Cheng, M. T., Ji, D. S., Liu, Z. R., Hu, B., Sun, Y., Wang, Y. S.: Characterization of submicron particles during biomass burning and coal combustion periods in Beijing, China. Sci. Total. Environ., 562, 812–821, https://dx.doi.org/10.1016/j.scitotenv.2016.04.015, 2016.

Zhang, G. H., Lian, X. F., Fu, Y. Z., Lin, Q. H., Li, L., Song, W., Wang, Z. Y., Tang, M. J., Chen, D. H., Bi, X. H., Wang, X. M., and Sheng, G. Y.: High secondary formation of nitrogen-containing organics (NOCs) and its possible link to oxidized organics and ammonium, Atmos. Chem. Phys., 20, 1469–1481, https://doi.org/10.5194/acp-20-1469-2020, 2020.

Zhang, X. H., Xu, J. Z., Kang, S. C., Zhang, Q., and Sun, J. Y.: Chemical characterization and sources of submicron aerosols in the northeastern Qinghai–Tibet Plateau: insights from high-resolution mass

https://doi.org/10.5194/acp-2022-786
Preprint. Discussion started: 16 December 2022

spectrometry, Atmos. Chem. Phys., 19, 7897−7911, https://doi.org/10.5194/acp-19-7897-2019, 2019a.

Zhang, N. N., Cao, J. J., Xu, H. M., and Zhu, C. S.: Elemental compositions of $PM_{2.5}$ and TSP in Lijiang, southeastern edge of Tibetan Plateau during pre-monsoon period, Particuology, 11(1), 63–69, https://doi.org/10.1016/j.partic.2012.08.002, 2013.

Zhang, S. P., Xing, J., Sarwar, G., Ge, Y. L., He, H., Duan, F. K., Zhao, Y., He, K. B., Zhu, L. D., Chu, B. W.: Parameterization of heterogeneous reaction of SO_2 to sulfate on dust with coexistence of NH_3 and NO_2 under different humidity conditions, Atmos. Environ., 208, 133–140, https://doi.org/10.1016/j.atmosenv.2019.04.004, 2019b.

Zhu, C. S., Cao, J. J., Hu, T. F., Shen, Z. X., Tie, X. X., Huang, H., Wang, Q. Y., Huang, R. J., Zhao, Z. Z., Mocnik, G., and Hansen, A.D.A.: Spectral dependence of aerosol light absorption at an urban and a remote site over the Tibetan Plateau, Sci. Total Environ., 591, 14–21, https://doi.org/10.1016/j.scitotenv.2017.03.057, 2017.

Zhao, S.Y., Tie, X.X., Long, X., and Cao, J.J.: Impacts of Himalayas on black carbon over the Tibetan Plateau during summer monsoon, Sci. Total Environ., 598, 307–318, https://doi.org/10.1016/j.scitotenv.2017.04.101, 2017.

https://doi.org/10.5194/acp-2022-786
Preprint. Discussion started: 16 December 2022

Atmospheric Chemistry and Physics
Discussions

Table 1. The number concentrations, average percentages and characteristic ions of nine types of particles during the entire study period, and the average percentages of the major six particle types during two episodes.

Type	Number count	Fraction in total (%)	Episode 1 (%)	Episode 2 (%)	Tracer ions
rich-K	151040	30.9	29.0	39.3	$^{39}K^+$, $^{26}CN^-$, $^{42}CNO^-$, $^{46}NO_2^-$, $^{62}NO_3^-$, $^{97}HSO_4^-$
BB	91322	18.7	11.5	14.2	$^{39}K^+$, levoglucosan ($^{45}CHO_2^-$, $^{59}C_2H_3O_2^-$, $^{71}C_3H_3O_2^-$, $^{73}C_3HO_3^-$), $^{26}CN^-$, $^{35,37}Cl^-$, $^{42}CNO^-$, $^{46}NO_2^-$, $^{62}NO_3^-$, $^{97}HSO_4^-$
OC	62446	12.8	8.1	10.0	$^{27}C_2H_3^+$, $^{37}C_3H^+$, $^{38}C_3H_2^+$, $^{39}K^+/C_3H_3^+$, $^{43}C_2H_3O^+$, $^{51}C_4H_3^+$, $^{26}CN^-$, $^{42}CNO^-$, $^{46}NO_2^-$, $^{62}NO_3^-$, $^{97}HSO_4^-$
Ammonium	58317	11.9	17.5	13.5	$^{12}C^+$, $^{18}NH_4^+$, $^{39}K^+$, $^{58}C_2H_5NHCH_2^+$, $^{97}HSO_4^-$, $^{195}H(HSO_4)_2^-$
EC-aged	53337	10.9	10.0	17.2	$C_n^{\pm}$ (n =1 ~ 5), $^{39}K^+$, $^{97}HSO_4^-$
Dust	52533	10.7	20.3	1.3	$^{40}Ca^+$, $^{56}CaO^+$, $^{16}O^-$, $^{17}OH^-$, $^{76}SiO_3^-$, $^{79}PO_3^-$
NaK-SN	13726	2.8	na	na	$^{23}Na^+$, $^{39}K^+$, $^{62}NO_3^-$, $^{97}HSO_4^-$
Metal	4672	1.0	na	na	$^{51}V^+$, $^{56}Fe^+$, $^{64,66,68}Zn^+$, $^{206,207,208}Pb^+$
Others	1580	0.3	na	na	No obvious characteristic peaks

https://doi.org/10.5194/acp-2022-786
Preprint. Discussion started: 16 December 2022

Figure captions:

Figure 1. Box and whisker diurnal plots of the number concentration of the main particle types (a) rich-Potassium (K), (b) Biomass burning (BB), (c) Organic carbon (OC), (d) Ammonium, (e) Element carbon (EC)-aged, (f) Dust in hourly resolution. The lower, middle, and upper lines of the boxes denote the 25th, 50th, and 75th percentiles. The lower and upper whiskers show the 10th and 90th percentiles, respectively. Average values are shown in white dots.

Figure 2. Maps of the mean HYSPLIT back trajectory clusters (72 h) at the height of 500 m during the whole field observation; the table embedded in the figure is the number concentration and relative fraction of the main six particle types in each cluster.

Figure 3. Size distributions of (a) the total number particle counts, (b) the relative percentages (%) of the total particles for nine groups during the sampling campaign.

Figure 4. Number fractions of secondary markers associated with the six particle types (rich-K, BB, OC, Ammonium, EC-aged, Dust). Secondary species include sulfate ($^{97}HSO_4^-$), sulfuric acid ($^{195}H(HSO_4)_2^-$), nitrate ($^{62}NO_3^-$), ammonium ($^{18}NH_4^+$), DEA (diethylamine, $^{58}C_2H_5NHCH_2^+$), and oxalate ($^{89}HC_2O_4^-$) ions.

Figure 5. Size distributions of the (a, c) number concentrations and (b, d) fractions of the major six particle types (rich-K, BB, OC, Ammonium, EC-aged, Dust) during two episodes of (a,b) E1 and (c, d) E2.

Figure 6. Number fractions of secondary markers associated with the six particle types (rich-K, BB, OC, Ammonium, EC-aged, Dust) in two episodes events of E1 and E2: sulfate ($^{97}HSO_4^-$), sulfuric acid ($^{195}H(HSO_4)_2^-$), nitrate ($^{62}NO_3^-$), ammonium ($^{18}NH_4^+$), DEA (diethylamine, $^{58}C_2H_5NHCH_2^+$), and oxalate ($^{89}HC_2O_4^-$).

Figure 7. Correlations between the relative number fractions of the secondary species (a) $^{43}C_2H_3O^+$, (b) $^{89}HC_2O_4^-$, (c) $^{18}NH_4^+$, (d) $^{62}NO_3^-$, (e) $^{97}HSO_4^-$ and O_x concentration during E1 (blue square) and E2 (red dot).

Figure 8. Correlations between the relative number fractions of the secondary species (a)

https://doi.org/10.5194/acp-2022-786
Preprint. Discussion started: 16 December 2022

Atmospheric Chemistry and Physics Discussions

$^{43}C_2H_3O^+$, (b) $^{89}HC_2O_4^-$, (c) $^{18}NH_4^+$, (d) $^{62}NO_3^-$, (e) $^{97}HSO_4^-$ and relative humidity (RH) during E1 (cyan dot) and E2 (orange square).

https://doi.org/10.5194/acp-2022-786
Preprint. Discussion started: 16 December 2022

Atmospheric Chemistry and Physics
Discussions

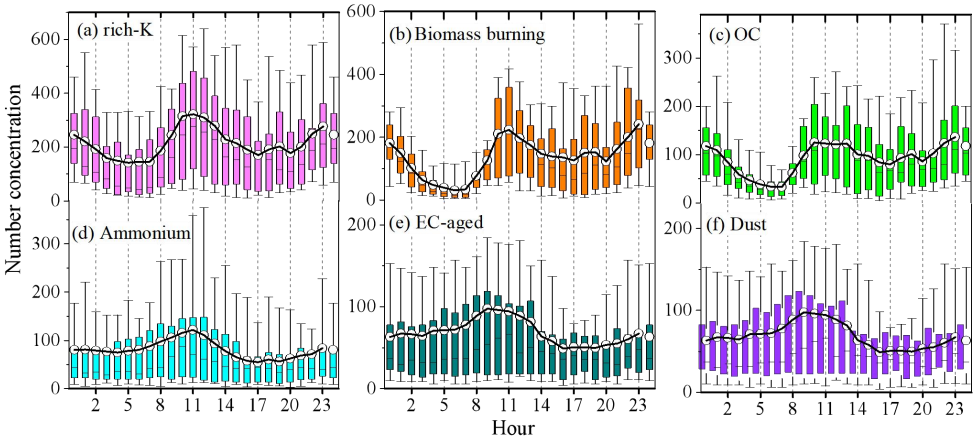

Figure 1. Box and whisker diurnal plots of the number concentration of the main particle types (a) rich-Potassium (K), (b) Biomass burning (BB), (c) Organic carbon (OC), (d) Ammonium, (e) Element carbon (EC)-aged, (f) Dust in hourly resolution. The lower, middle, and upper lines of the boxes denote the 25th, 50th, and 75th percentiles. The lower and upper whiskers show the 10th and 90th percentiles, respectively. Average values are shown in white dots.

https://doi.org/10.5194/acp-2022-786
Preprint. Discussion started: 16 December 2022

Atmospheric Chemistry and Physics
Discussions

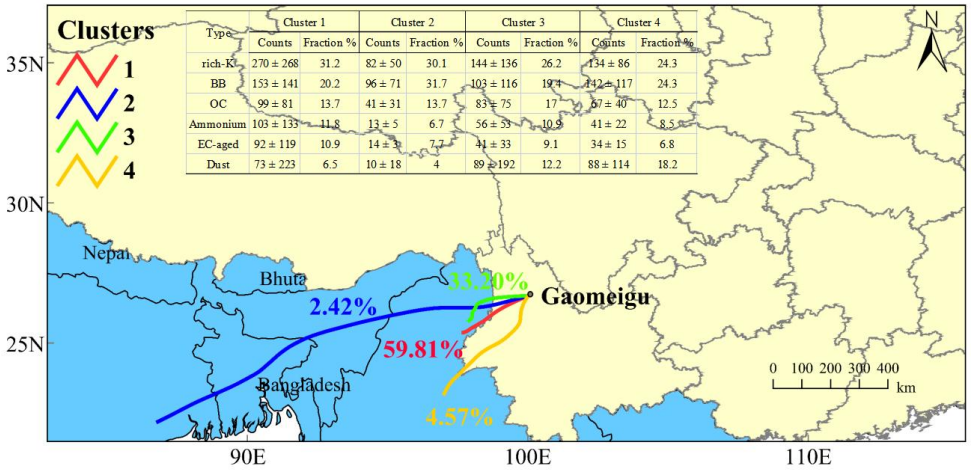

Type	Cluster 1		Cluster 2		Cluster 3		Cluster 4	
	Counts	Fraction %	Counts	Fraction %	Counts	Fraction %	Counts	Fraction %
rich-K+	270 ± 268	31.2	82 ± 50	30.1	144 ± 136	26.2	134 ± 86	24.3
BB	153 ± 141	20.2	96 ± 71	31.7	103 ± 116	19.1	142 ± 117	24.3
OC	99 ± 81	13.7	41 ± 31	13.7	83 ± 75	17	67 ± 40	12.5
Ammonium	103 ± 133	11.8	13 ± 5	6.7	56 ± 53	10.9	41 ± 22	8.5
EC-aged	92 ± 119	10.9	14 ± 3	7.7	41 ± 33	9.1	34 ± 15	6.8
Dust	73 ± 223	6.5	10 ± 18	4	89 ± 192	12.2	88 ± 114	18.2

Figure 2. Maps of the mean HYSPLIT back trajectory clusters (72 h) at the height of 500 m during the whole field observation; the table embedded in the figure is the number concentration and relative fraction of the main six particle types in each cluster.

https://doi.org/10.5194/acp-2022-786
Preprint. Discussion started: 16 December 2022

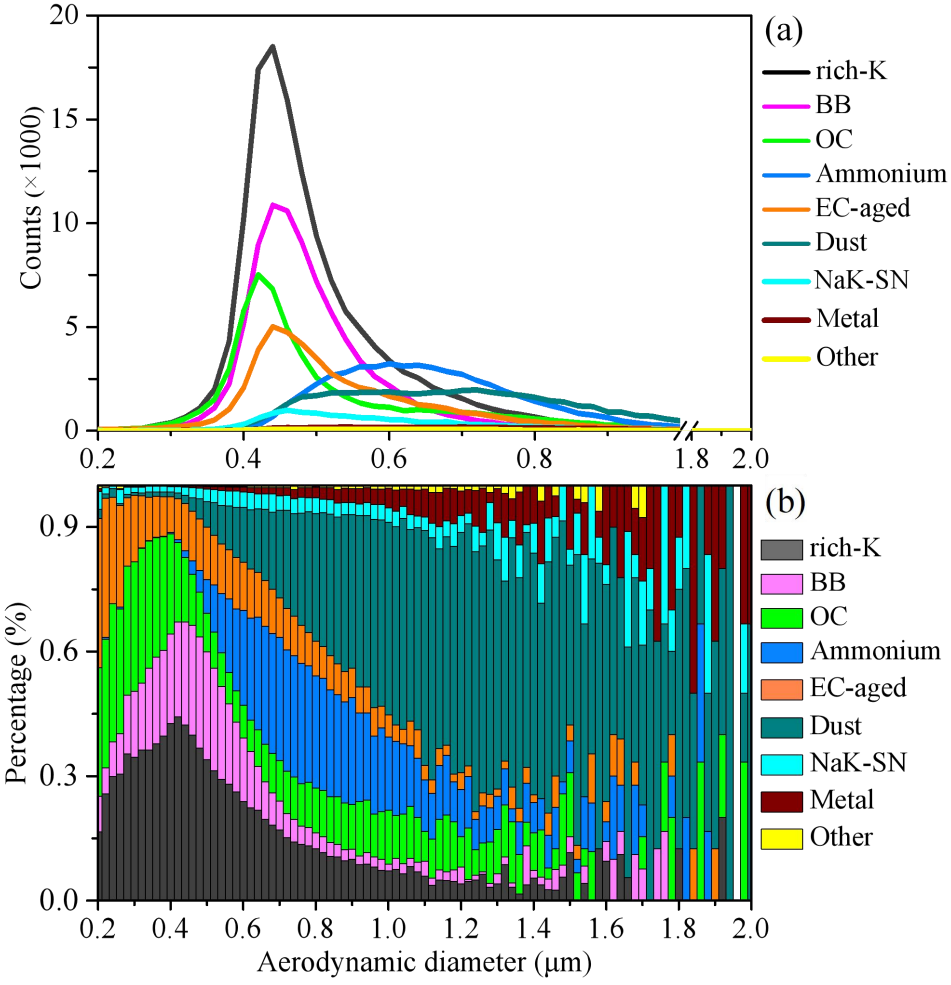

Figure 3. Size distributions of (a) the total number particle counts, (b) the relative percentages (%) of the total particles for nine groups during the sampling campaign.

https://doi.org/10.5194/acp-2022-786
Preprint. Discussion started: 16 December 2022

Atmospheric Chemistry and Physics
Discussions

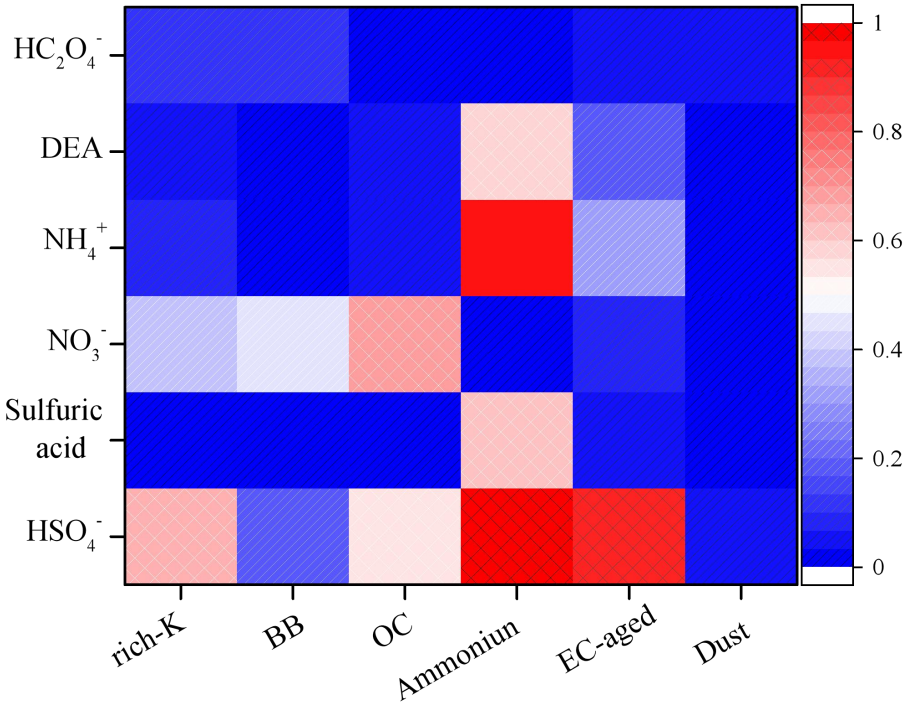

Figure 4. Number fractions of secondary markers associated with the six particle types (rich-K, BB, OC, Ammonium, EC-aged, Dust). Secondary species include sulfate ($^{97}HSO_4^-$), sulfuric acid ($^{195}H(HSO_4)_2^-$), nitrate ($^{62}NO_3^-$), ammonium ($^{18}NH_4^+$), DEA (diethylamine, $^{58}C_2H_5NHCH_2^+$), and oxalate ($^{89}HC_2O_4^-$) ions.

https://doi.org/10.5194/acp-2022-786
Preprint. Discussion started: 16 December 2022

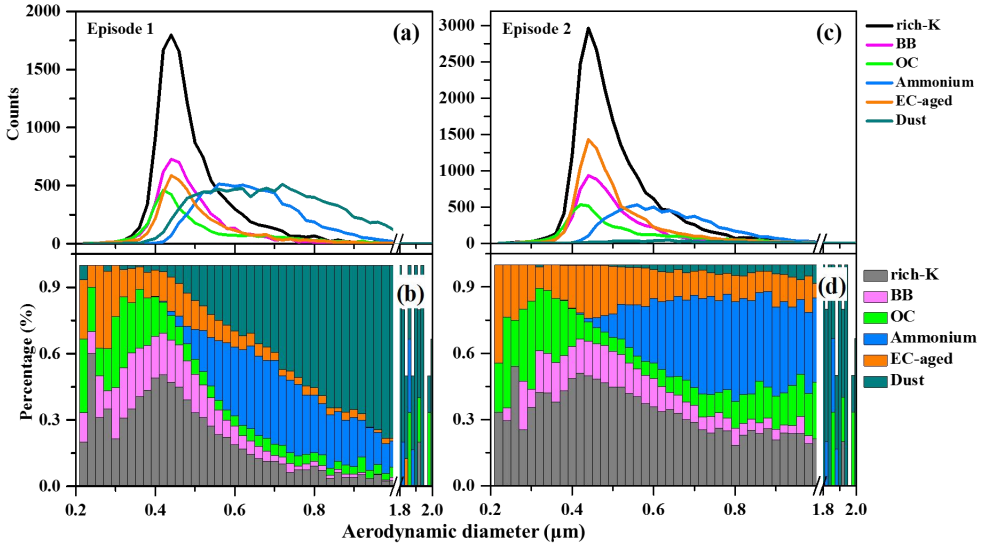

Figure 5. Size distributions of the (a, c) number concentrations and (b, d) fractions of the major six particle types (rich-K, BB, OC, Ammonium, EC-aged, Dust) during two episodes of (a,b) E1 and (c, d) E2.

https://doi.org/10.5194/acp-2022-786
Preprint. Discussion started: 16 December 2022

Atmospheric Chemistry and Physics Discussions
Open Access

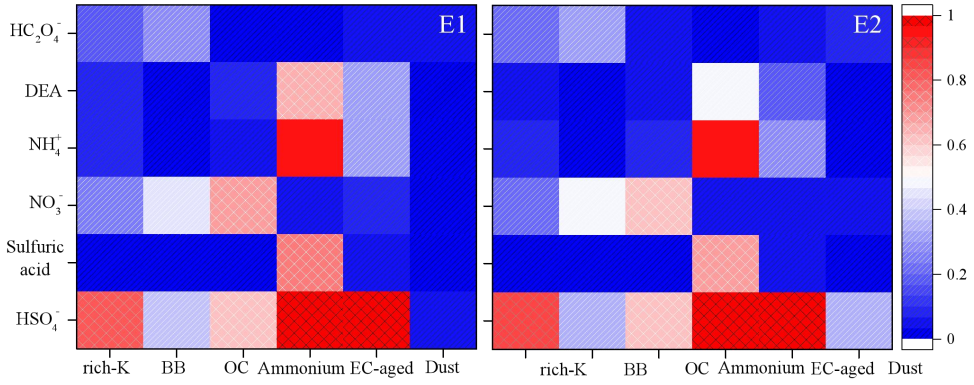

Figure 6. Number fractions of secondary markers associated with the six particle types (rich-K, BB, OC, Ammonium, EC-aged, Dust) in two episodes events of E1 and E2: sulfate ($^{97}HSO_4^-$), sulfuric acid ($^{195}H(HSO_4)_2^-$), nitrate ($^{62}NO_3^-$), ammonium ($^{18}NH_4^+$), DEA (diethylamine, $^{58}C_2H_5NHCH_2^+$), and oxalate ($^{89}HC_2O_4^-$).

https://doi.org/10.5194/acp-2022-786
Preprint. Discussion started: 16 December 2022

Atmospheric Chemistry and Physics
Discussions

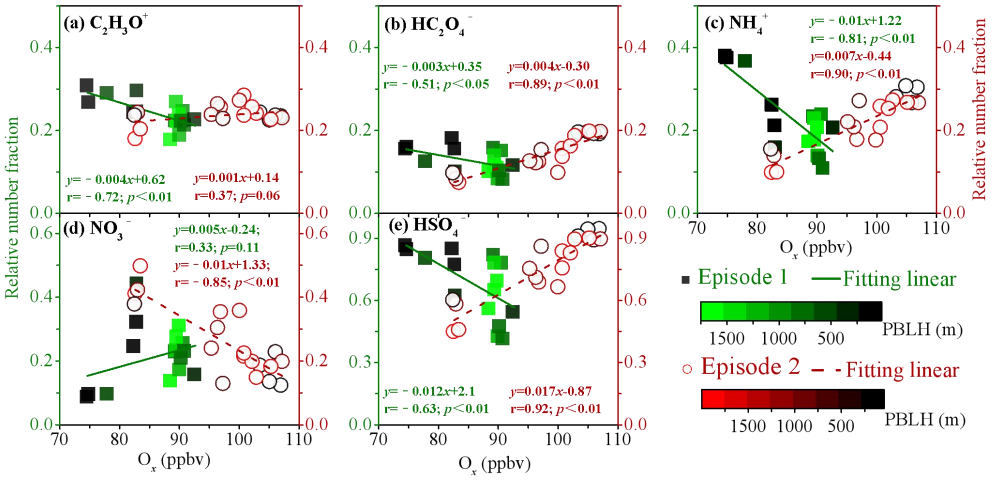

Figure 7. Correlations between the relative number fractions of the secondary species (a) $^{43}C_2H_3O^+$, (b) $^{89}HC_2O_4^-$, (c) $^{18}NH_4^+$, (d) $^{62}NO_3^-$, (e) $^{97}HSO_4^-$ and O_x concentration during E1 (blue square) and E2 (red dot).

https://doi.org/10.5194/acp-2022-786
Preprint. Discussion started: 16 December 2022

Atmospheric Chemistry and Physics Discussions
Open Access

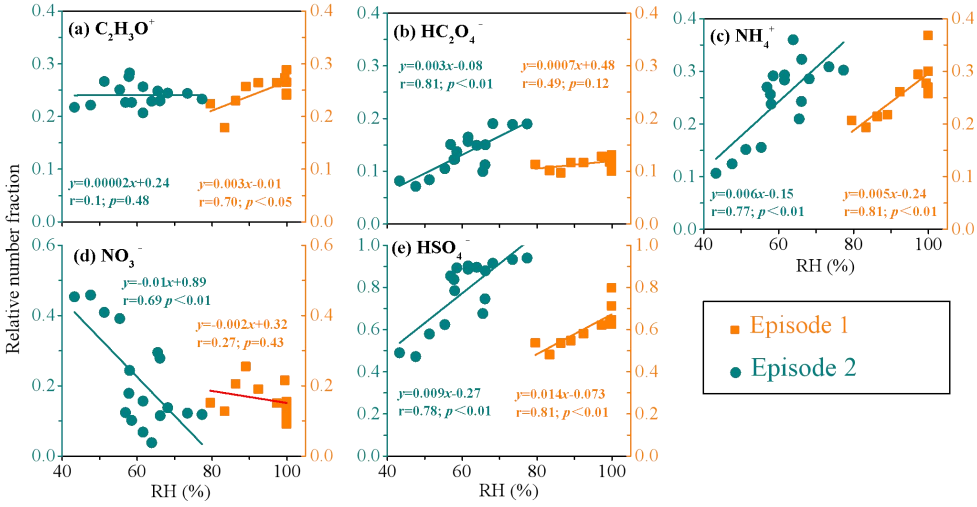

Figure 8. Correlations between the relative number fractions of the secondary species (a) $^{43}C_2H_3O^+$, (b) $^{89}HC_2O_4^-$, (c) $^{18}NH_4^+$, (d) $^{62}NO_3^-$, (e) $^{97}HSO_4^-$ and relative humidity (RH) during E1 (cyan dot) and E2 (orange square).